

<https://doi.org/10.1038/s42005-026-02497-8>

Visualizing electronic structure of twisted bilayer MoTe₂ in devices

Check for updates

Cheng Chen^{1,9}, William Holtzmann^{2,9}, Xiao-Wei Zhang^{3,9}, Eric Anderson², Shanmei He¹, Yuzhou Zhao^{2,3}, Weijie Li², Jieyi Liu^{1,4}, Yucheng Guo^{5,6}, Chris Jozwiak⁵, Aaron Bostwick⁵, Eli Rotenberg⁵, Kenji Watanabe⁷, Takashi Taniguchi⁸, Ting Cao³, Di Xiao^{2,3}, Xiaodong Xu^{2,3} & Yulin Chen¹ ✉

The pursuit of emergent quantum phenomena lies at the forefront of modern condensed matter physics. A recent breakthrough in this arena is the discovery of the fractional quantum anomalous Hall effect (FQAHE) in twisted bilayer MoTe₂ (tbMoTe₂), marking a paradigm shift and establishing a versatile platform for exploring the intricate interplay among topology, magnetism, and electron correlations. While significant progress has been made through both optical and electrical transport measurements, direct experimental insights into the electronic structure – crucial for understanding and modeling this system – have remained elusive. Here, using spatially and angle-resolved photoemission spectroscopy (μ -ARPES), we directly map the electronic band structure of tbMoTe₂. We identify the valence band maximum, whose partial filling underlies the FQAHE, at the K points, situated approximately 150 meV above the Γ valley. By fine-tuning the doping level via in-situ alkali metal deposition, we also resolve the conduction band minimum at the K point, providing direct evidence that tbMoTe₂ exhibits a direct band gap – distinct from all previously known moiré bilayer transition metal dichalcogenide systems. These results offer critical insights for theoretical modeling and advance our understanding of fractionalized excitations and correlated topological phases in this emergent quantum material.

The exploration of exotic quantum phenomena and emergent electronic states in two-dimensional (2D) materials has fueled a vibrant and rapidly advancing field in condensed matter physics¹. Among these, twisted bilayer moiré systems have attracted intense interest as fertile platforms for uncovering novel electronic behavior^{2–5}. Twist-induced moiré patterns can dramatically alter electronic properties, giving rise to remarkable phenomena such as unconventional superconductivity in magic-angle twisted bilayer graphene (MATBG)^{6,7}, and more recently, the observation of the fractional quantum anomalous Hall effect (FQAHE) in R-stacked twisted bilayer MoTe₂ (tbMoTe₂)^{8–11}. The FQAHE—marked by the quantization of the anomalous Hall conductance at fractional values of the elementary charge—exemplifies a topologically nontrivial phase governed by strong electron correlations^{12–15}. Understanding the underlying band structure of tbMoTe₂ is thus crucial for unraveling the mechanisms behind this exotic

state and opens new avenues for both fundamental studies and potential technological applications.

In this study, we report a direct measurement of the electronic band structure of tbMoTe₂ with a 4° twist angle (the angle when FQAHE occurs) using angle-resolved photoemission spectroscopy with sub-micrometre spatial resolution (μ -ARPES). Over the past decade, μ -ARPES has emerged as a powerful technique for probing the electronic structures of 2D materials and their heterostructures^{16–18}. However, most prior studies have focused on air-stable materials, such as graphene-based devices—including MATBG^{19–22}—and stable transition metal dichalcogenides (TMDs)^{23–28}. In contrast, devices based on air-sensitive materials like tbMoTe₂ are typically encapsulated with inert, stable layers such as graphene to prevent degradation. While graphene encapsulation is compatible with μ -ARPES by allowing photoelectrons to escape with ~30% efficiency through a monolayer

¹Department of Physics, University of Oxford, Oxford, UK. ²Department of Physics, University of Washington, Seattle, WA, USA. ³Department of Materials Science and Engineering, University of Washington, Seattle, WA, USA. ⁴Diamond Light Source, Harwell Science and Innovation Campus, Didcot, UK. ⁵Advanced Light Source, Lawrence Berkeley National Laboratory, Berkeley, CA, USA. ⁶Department of Physics and Astronomy, Rice University, Houston, TX, USA. ⁷Research Center for Functional Materials, National Institute for Materials Science, Tsukuba, Japan. ⁸International Center for Materials Nanoarchitectonics, National Institute for Materials Science, Tsukuba, Japan. ⁹These authors contributed equally: Cheng Chen, William Holtzmann, Xiao-Wei Zhang.

✉ e-mail: yulin.chen@physics.ox.ac.uk

graphene capping²⁹, and has been successfully applied to few-layer WTe_2 ^{30,31}, it remains incompatible with transport measurements and may introduce extrinsic effects such as strong dielectric screening and charge transfer, potentially obscuring the intrinsic electronic structures that give rise to the correlated topological states of the encapsulated material. Instead, here we employ monolayer hexagonal boron nitride (hBN) to encapsulate the tbMoTe_2 device. Owing to its wide band gap (~ 5.9 eV) and minimal thickness (~ 0.3 nm), monolayer hBN enables efficient photoelectron transmission in μ -ARPES measurements while preserving the intrinsic electronic structure of tbMoTe_2 .

Result

Measurement schematic and sample geometry

A schematic of the μ -ARPES setup and device configuration is shown in Fig. 1a. The tbMoTe_2 device was fabricated entirely within an inert glovebox environment, with a partially overlapping graphene flake serving as an electrical ground (see “Methods” and Fig. S1 for fabrication details). The device is fully encapsulated between a monolayer hBN top layer and a ~ 12 nm thick hBN bottom layer (Fig. 1a). Consistent with the optical image of the device (Fig. 1b(i)), the μ -ARPES spectral intensity integrated around the Fermi level (E_F) from real-space scanning (Fig. 1b(ii)) enables clear identification of regions with distinct conductivity, including gold contacts, the SiO_2/Si substrate, and hBN flakes. A higher-resolution scan of the sample area (Fig. 1b(iv)) further employs the characteristic Te-4d level photoemission signal to precisely locate the tbMoTe_2 region. The band structures of monolayer MoTe_2 and tbMoTe_2 , shown in Figs. 2 and 3, were acquired at the spatial locations labeled as P1 and P2 in Fig. 1b(iv), respectively.

General electronic band structure

Remarkably, photoelectrons from the underlying MoTe_2 sample can also penetrate the monolayer hBN encapsulation layer efficiently, enabling high-quality ARPES measurements. Figure 2 displays well-resolved band dispersions for both monolayer MoTe_2 and tbMoTe_2 . The 3D spectral plot (Fig. 2a) and constant energy contour (Fig. 2b) reveal the overall band structure within the first Brillouin zone (BZ), with the most prominent differences observed near the Γ point. To highlight the distinctions between monolayer and twisted bilayer MoTe_2 , detailed band dispersions along the

$M-\Gamma-K$ high-symmetry directions in the BZ are presented in Fig. 2c. At the Γ point, monolayer MoTe_2 exhibits a characteristic flat valence band top (Fig. 2c, top row). In contrast, tbMoTe_2 shows a pronounced upward shift of the valence band due to strong interlayer coupling, resulting in a dome-shaped valence band maximum (Fig. 2c, bottom row). At the K point, however, the band structures of both systems remain mostly similar, indicating small twist-induced modifications in that region of momentum space.

The different behavior at Γ and K points can be understood based on the orbital components of the bands at these two points (Fig. S2), respectively: In each constituent MoTe_2 layer, the K-valley bands are contributed by orbitals with in-plane spatial extensions ($\text{Mo } d_{xy}, d_{x^2-y^2}$ and smaller contributions from $\text{Te } p_x, p_y$ orbitals), which are weakly coupled between layers due to the small interlayer overlap of their wave functions; while for Γ valley, the bands are formed by $\text{Mo } d_{z^2}$ and $\text{Te } p_z$ orbitals, which naturally have more out-of-plane extensions and larger overlap (thus stronger interlayer coupling), similar to the situation in twisted bilayer WSe_2 system²³.

The high-resolution measurements further enable the extraction of key band structure parameters. As shown in Fig. 2d, the valence band maximum (VBM) is located at the K point in both monolayer and tbMoTe_2 (see Fig. S3 for its robustness). Compared to monolayer MoTe_2 (Fig. 2d, top row), the valence band near the Γ point in tbMoTe_2 (Fig. 2d, bottom row) is significantly elevated due to interlayer coupling, bringing it closer in energy to the VBM at K. The identification of the VBM at the K point is the first step towards determining the magnitude and location of the band gap in tbMoTe_2 .

Probing conduction band via in-situ dosing

To locate the conduction band minimum (CBM) of both MoTe_2 and tbMoTe_2 , we need to probe the unoccupied bands above the E_F . The electrostatic-gating ARPES measurement remains technically challenging in these air-sensitive and semiconducting 2H-phase TMDs systems, mainly due to the insufficiency of one-side gating and the high metal-semiconductor contact resistance. Alternatively, we adopted the widely used in-situ alkali metal dosing in ARPES measurement, which is both more convenient and effective in visualizing the unoccupied states¹⁷. Remarkably, this method is effective even in our monolayer hBN-encapsulated device

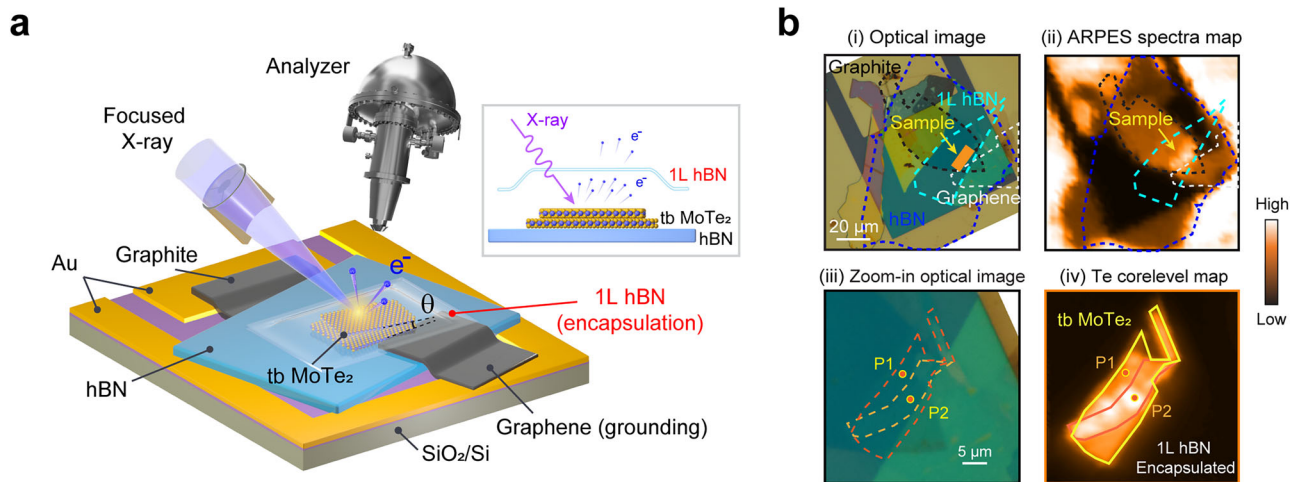


Fig. 1 | μ -ARPES measurement and twisted bilayer MoTe_2 device geometries. **a** Schematic of the experiment setup. The twisted bilayer (tb) MoTe_2 sample (4° twist) is fully encapsulated/protected by a monolayer hexagonal boron nitride (hBN), and electronically grounded through a graphene/gold electrode. hBN/graphite backgate is also incorporated in this device (but not activated in the current study). **b** Real-space information of the device. (i) Optical microscope image and (ii) corresponding ARPES spectral intensity map. The shape of encapsulation monolayer hBN, graphene electrode, and hBN/graphite backgate are indicated,

respectively. (iii) Zoomed-in optical microscope image of the tbMoTe_2 device. Top/bottom MoTe_2 layers are highlighted with orange/yellow lines, and P1/ P2 indicates the spatial position of monolayer/twisted bilayer, where the μ -ARPES experiments were performed. (iv) Photoemission intensity map from Te-4d levels ($E_b = 40.4$ and 41.9 eV for $\text{Te-4d}_{5/2}$ and $\text{Te-4d}_{3/2}$, respectively), highlighting the tbMoTe_2 sample. μ -ARPES: angle-resolved photoemission spectroscopy with sub-micrometre spatial resolution.

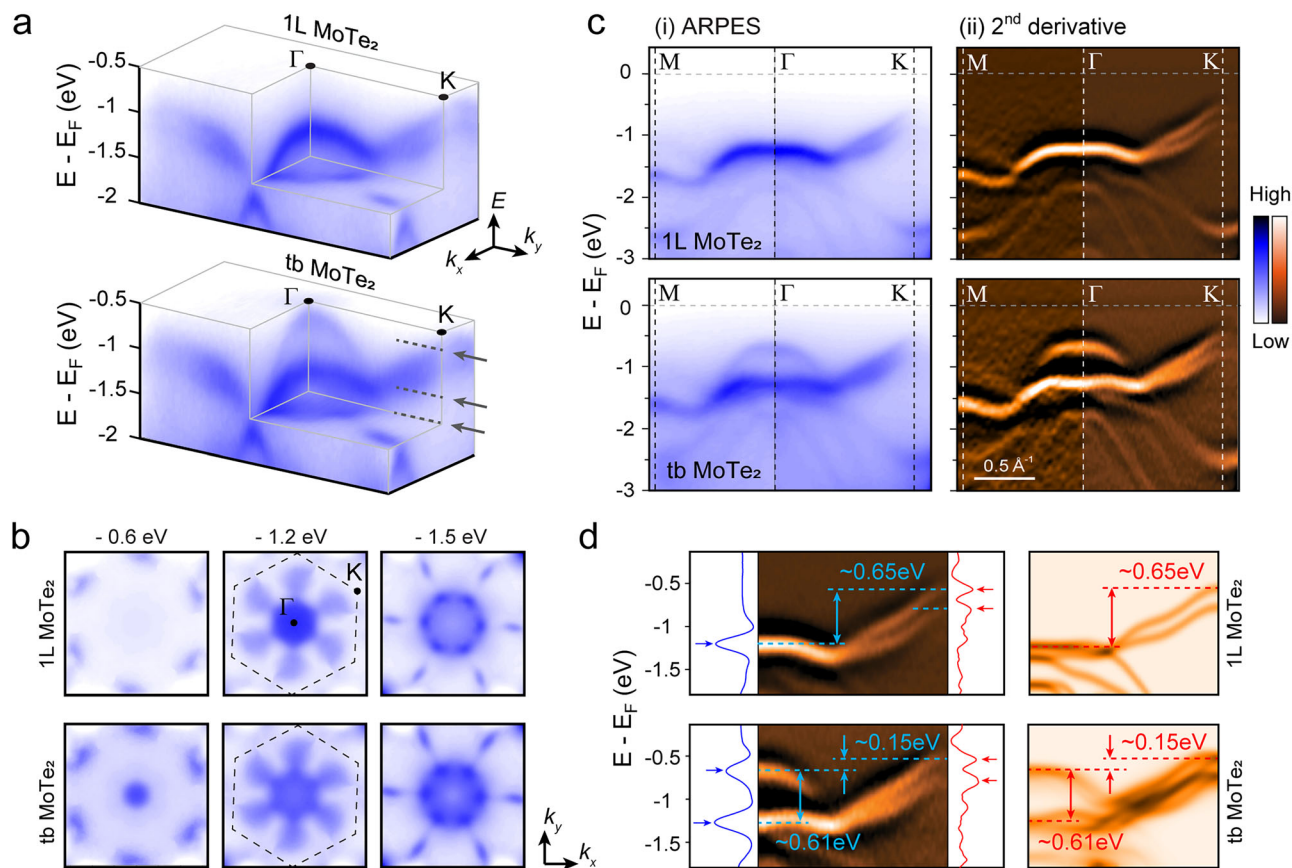


Fig. 2 | General electronic structure of monolayer and twisted bilayer MoTe₂. **a** Volume plot of photoemission intensity for monolayer (1 L) MoTe₂ and twisted bilayer (tb) MoTe₂. High symmetry points Γ and K in the Brillouin Zone (BZ) are labelled. E_F energy of Fermi level. **b** Constant energy contours of the photoemission maps at binding energies of -0.6 eV, -1.2 eV, and -1.5 eV, for 1 L MoTe₂ and tb MoTe₂, respectively. The BZ and Γ , and K points are overlaid. **c** (i) ARPES band

dispersion plot and (ii) corresponding second partial derivative plot, along $M-\Gamma-K$ directions. **d** Zoomed-in details of the band parameters (left column) and its comparison with theoretical calculation (right column). The intensity as a function of energy at both Γ (blue curve) and K (red curve) points are plotted on the side, with the band positions marked by the arrows.

(Fig. 3a), and we observed the CBM emerging at the K point (Fig. 3b, c), with an estimated direct band gap of ~ 1.1 eV for both MoTe₂ and tbMoTe₂. On the other side, the photoluminescence (PL) experiment on a tbMoTe₂ device (with top gate) also illustrates prominent signals from both exciton and trion excitations (Fig. 3d, e). These evidences unambiguously confirm the direct band gap nature of tbMoTe₂, making it a rare case in moiré system based on 2H-TMDs. This is crucial for realizing exotic emergent phenomena, such as FQAHE, related to K-valley moiré physics^{32,33}. It is worth noting that the observed band gap in ARPES is comparable to the exciton energy in PL, but slightly less - this phenomenon can be attributed to the renormalization of the quasiparticle band gap, which has been observed in both alkali metal doping and electrostatic-gating ARPES experiments^{34,35}. In a semiconductor, this effect is expected to occur due to the free-carrier screening effect³⁶.

Theoretical calculation of band structure

To gain a more comprehensive understanding of the electronic structure of tbMoTe₂, we performed first-principles calculations within the framework of Kohn-Sham density functional theory (DFT). The calculated band structures for monolayer MoTe₂, R-stacked bilayer MoTe₂, and tbMoTe₂ are presented and compared in Fig. 4. For monolayer MoTe₂, the calculations reveals a direct band gap at the K point of the Brillouin zone (Fig. 4a(i)), in excellent agreement with our experimental results (Figs. 2c and 3c, and ref. 37). For both R-stacked bilayer and tbMoTe₂ (Fig. 4a(ii, iii)), the valence band maximum at the Γ point is significantly elevated, consistent with the experimental data (Figs. 2c and 3c). However, the CBM in both bilayer configurations is predicted to shift away from the K point to an off-

symmetry location (denoted as Q; Fig. 4a(ii, iii)), in clear contrast to our ARPES measurements, which reveal the CBM to reside at the K point (Fig. 3c).

The DFT calculated energy positions of K and Q valleys are sensitive to many factors, such as the choice of lattice constant and the pseudopotential used^{38,39}, making the calculation unreliable in determining the actual band alignment. This is why the experimental result, such as the ARPES data presented above, is crucial. Nevertheless, to address this discrepancy between calculation and experiment, and also to showcase the influence of lattice parameter, we investigated the effect of potential in-plane strain on the band alignment. As illustrated in Fig. 4b, the local CBM at the Q point shifts upward relative to the K point with a biaxial strain of 1%. This behavior can be understood by considering the orbital components contributing to the conduction band. At the K point, the conduction band states are dominated by d_{z^2} , whereas at the Q valley, they have a more mixed orbital character, including d_{xy} , $d_{x^2-y^2}$, and some chalcogen p orbitals. As a result, the K valley is less sensitive to in-plane lattice expansion, but the Q valley shifts upwards more significantly. We found that with 1% of biaxial strain, we can align the CBM at the K point. It is worth noting, the real situation is more complex. Factors such as local strain, lattice distortion, and corrugation will need careful investigation in future works.

Discussion

The successful extraction of the electronic band structure of tbMoTe₂ within a functional device with key band parameters derived from both our μ -

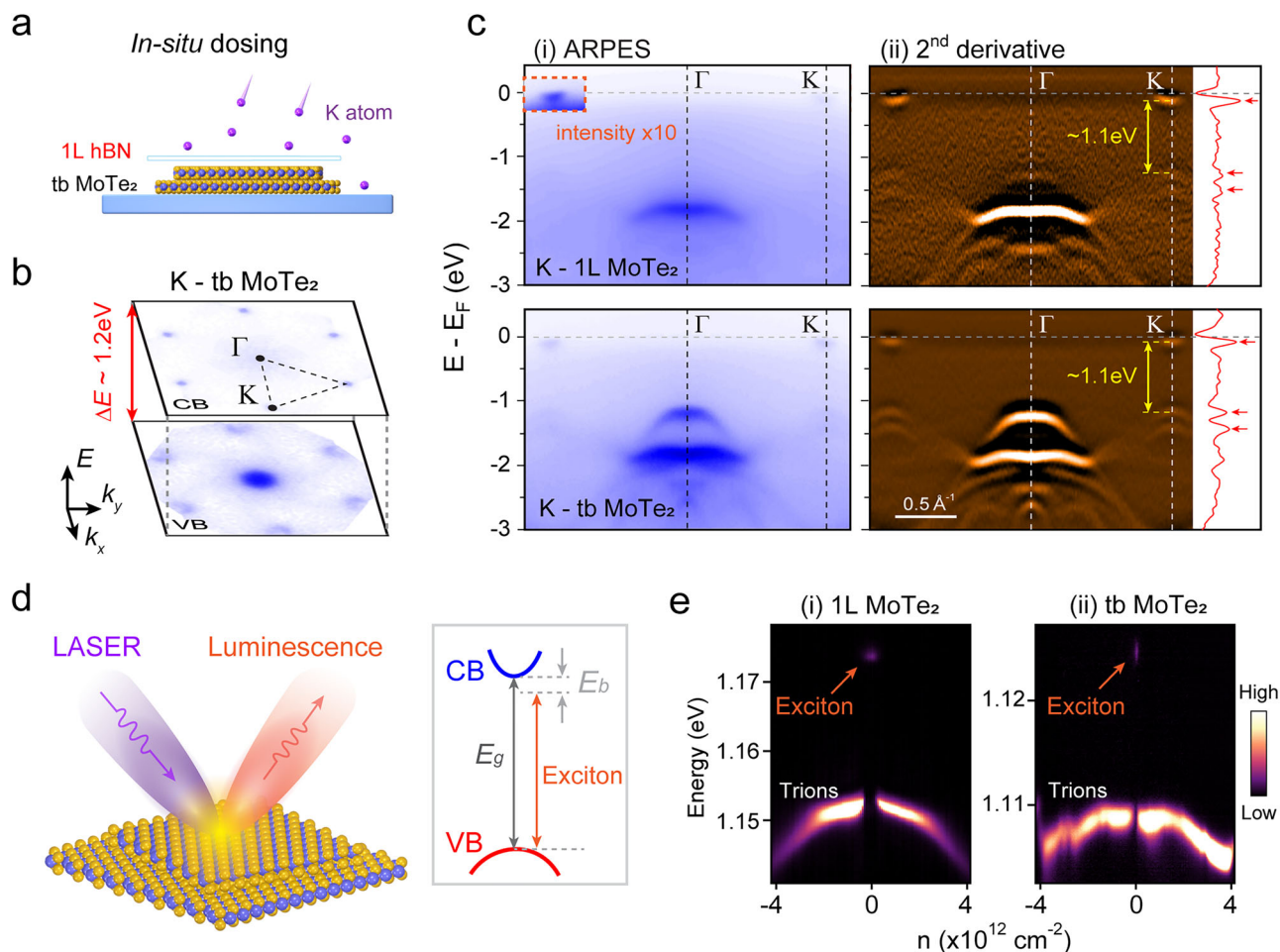


Fig. 3 | Direct band gap in monolayer and twisted bilayer MoTe₂. **a** Illustration of in-situ potassium surface dosing, which introduces additional electron carriers into the sample. **b** Slices plot of constant energy contours of tbMoTe₂ after potassium surface dosing, showing the positions of conduction bands (CB) and valence bands (VB). **c** (i) ARPES band dispersion plot and (ii) corresponding second partial derivative plot, along Γ –K direction of monolayer (top row) and tbMoTe₂ (bottom row), after potassium surface dosing. The intensity as a function of energy is plotted

on the side in (ii), where the band positions are marked by arrows. **d** Schematic of photoluminescence (PL) measurement and the generation of exciton. E_g band gap size, E_b exciton binding energy. However, the observed E_g in ARPES is suppressed, likely due to the free-carrier screening effect, making it comparable with the exciton energy. **e** PL intensity as a function of carrier density n , taken on (i) monolayer MoTe₂ and (ii) tbMoTe₂ devices (3.6° twist).

ARPES measurements (Fig. S4) and DFT calculations (see Table 1), represents a significant step forward in elucidating the detailed electronic structure of this system. A clear signature of moiré or flat bands at both the Γ and K points is still beyond the reach of our current resolution. Compared with the twisted bilayer WSe₂ system, where the signature of moiré bands at the Γ point is evidenced in ARPES measurements^{23,40}, spectroscopic investigation on the moiré effect of tbMoTe₂ presents more challenges. This is likely due to the higher instability of telluride compared to selenide, which not only reduces intrinsic sample/device quality but also necessitates the use of a top encapsulation layer. This results in an overall reduction of the statistics and energy resolution of the current ARPES measurement.

Looking ahead, we anticipate that future spectroscopic investigations—featuring higher energy and momentum resolution, improved statistical accuracy, and optimized device quality—will provide deeper insights into this moiré-engineered quantum system. Feasible improvements include the use of conventional high-resolution ARPES systems on larger samples to gain higher measurement throughput and better energy/momentum resolution; in situ sample fabrication method in vacuum¹⁸ to avoid both the use of encapsulation layer and air-exposure/vacuum-annealing process; the use of single crystal with improved crystal quality⁴¹, etc. Future investigation is expected to not only delineate detailed moiré band structure on a single particle level, but also the complex interplay among lattice, topology, and strong correlations, where the exotic emergent phenomena such as FQAHE originate.

In addition, this work demonstrates the technical feasibility of performing high-resolution μ -ARPES on hBN-encapsulated tbMoTe₂ devices, establishing a robust and non-invasive approach for probing the electronic structure of air-sensitive two-dimensional materials. Furthermore, the successful implementation of in-situ potassium dosing through the top hBN layer showcases a versatile and effective strategy for tuning the E_F and engineering the band structure *in operando*, particularly in situations where electrostatic gating is either impractical or insufficient. We anticipate that the distinctive capabilities of μ -ARPES will find widespread use in investigating the microscopic mechanisms of exotic quantum phenomena in moiré systems.

Note added

During the preparation of this manuscript, we became aware of a related ARPES study on twisted MoTe₂⁴².

Methods

Sample fabrication

To fabricate the device, hBN and graphite flakes were first exfoliated onto SiO₂/Si substrates and characterized using contrast-enhanced optical microscopy and atomic force microscopy (AFM). Then the bottom gate structure was fabricated using a standard poly-(bisphenol A) carbonate (PC)-based dry transfer process. A hBN flake as the bottom gate dielectric was picked up, successively followed by a graphite bottom gate electrode and

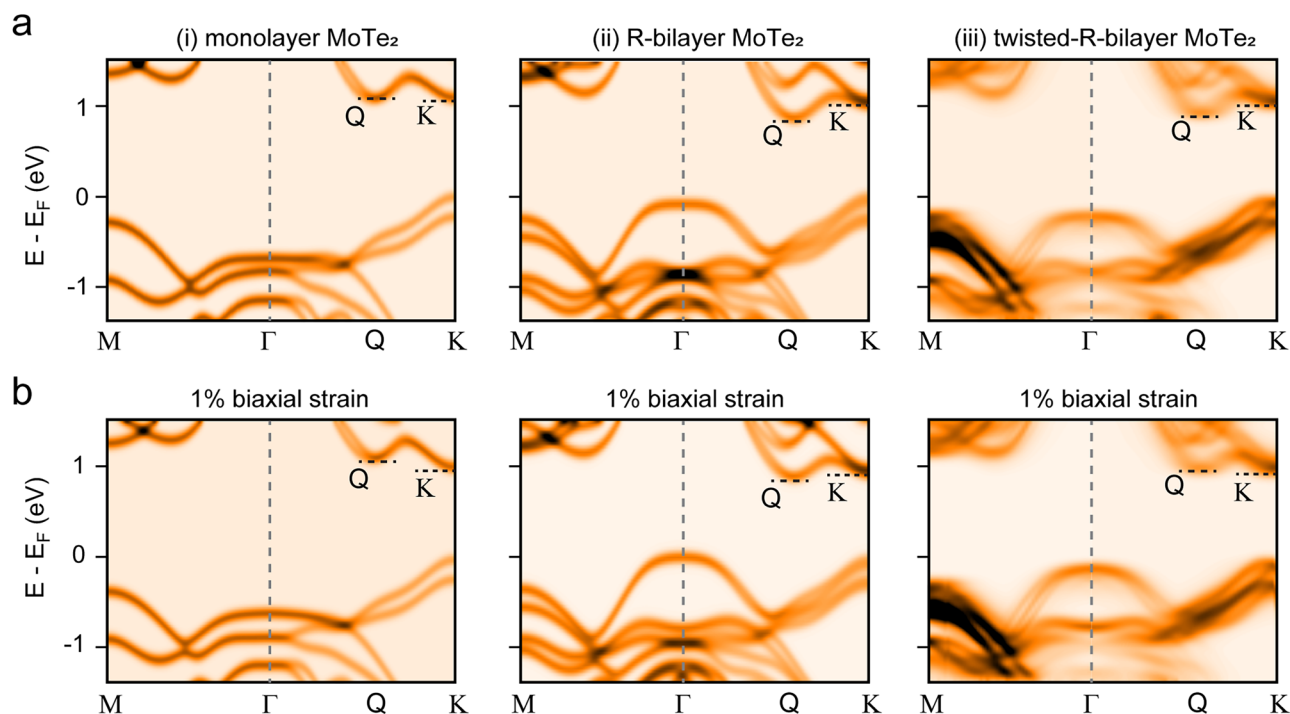


Fig. 4 | DFT calculated band structure. **a** Calculated band structure along $M-\Gamma-K$ directions for (i) monolayer, (ii) R-bilayer, and (iii) twisted(3.89°)-R-bilayer MoTe_2 . **b** Calculated band structure with a biaxial strain of 1%.

Table 1 | Band parameters of monolayer MoTe_2 and tbMoTe_2 , extracted from experimental results and theoretical calculations

		E_g (eV)	$E_K - E_\Gamma$ (eV)	Δ_{hy} (eV)	Δ_{so} (eV)	m_Γ^*/m_0	m_K^*/m_0
Monolayer MoTe_2	ARPES	1.1	0.65	-	0.24	15.4	0.74
	Calc.	1.1	0.67	-	0.22	11.2	0.66
4° tbMoTe_2	ARPES	1.1	0.15	0.61	0.28	1.84	0.67
	Calc.	1.03	0.17	0.62	0.22	2.18	-

E_g direct bandgap at K point, $E_K - E_\Gamma$ difference between the valence-band edges at K and Γ , Δ_{hy} Splitting of the valence band at Γ caused by interlayer hybridization, Δ_{so} Splitting of the valence band at K caused by spin-orbital coupling. m_Γ^*/m_0 : Effective mass of the valence-band edge at Γ /K in units of the free electron mass m_0 .

melted down onto a 285 nm SiO_2/Si substrate with pre-patterned Cr/Au (7/70 nm) electrodes via standard electron beam lithography. Next, MoTe_2 flakes were exfoliated onto a 285 nm SiO_2/Si inside a glovebox with O_2 and H_2O levels less than 0.1 ppm. A monolayer MoTe_2 flake was cut in half using an AFM tip before the transfer to minimize strain. The tbMoTe_2 heterostructure was created by picking up part of the monolayer MoTe_2 with the monolayer hBN encapsulation layer, rotating the transfer stage by a desired angle, and picking up the remaining flake. A graphene flake is also picked up, partially overlapped with tbMoTe_2 as a grounding electrode. The stack was then placed down on the prepared and cleaned backgate, such that the grounding graphene flake was electrically connected to the deposited contacts. The heterostructure geometry allows for full hBN encapsulation of the air-sensitive MoTe_2 . The stamp polymer was dissolved in anhydrous chloroform for 5 min and washed by anhydrous isopropyl alcohol inside a glovebox. The sample surface was further cleaned by an AFM (Bruker Edge) in contact mode.

Spatial- and angle-resolved photoemission spectroscopy (μ -ARPES)

Synchrotron-based μ -ARPES measurements were performed at Beamline 7.0.2 (MAESTRO) of the Advanced Light Source (ALS), USA. The samples were annealed in ultra-high vacuum at 220°C for 3 h (stability of the twist angle see SI Fig. S5) and measured under ultra-high vacuum below 3×10^{-11} Torr. The photon energy of the incident beam is 95 eV (Fig. 2) and 70 eV

(Fig. 3), and the measurement was performed at a temperature of 20 K. Data was collected using a R4000 analyser upgraded with deflectors. The incoming photon beam was focused down to $2 \mu\text{m}$ spot size by using a capillary mirror. The total energy and angle resolutions were 20 meV and 0.1° , respectively.

Optical measurement

Photoluminescence measurements were performed in reflection geometry in a home-built confocal optical microscope system. The sample was mounted in an exchange-gas cooled cryostat (attoDRY 2100) with a 9T superconducting magnet in Faraday geometry. A 632.8 nm HeNe laser was used as excitation for the photoluminescence measurements. The FWHM of the diffraction-limited excitation beam spot was $\sim 1 \mu\text{m}$. Photoluminescence signals were dispersed with a 600 grooves/mm diffraction grating blazed at $1 \mu\text{m}$ and detected using an LN-cooled InGaAs photodiode array (Princeton Instruments PyLoN-IR 1.7). A long pass filter was used to remove the excitation laser from the photoluminescence signal before entrance into the spectrometer.

Theoretical calculation

The lattice relaxations of the moiré superlattice were performed using the neural network (NN) potential. The NN potential was parameterized using the deep potential molecular dynamics (DPMD) method^{43,44}. The training datasets were generated from 5000-step ab initio molecular dynamics

simulations (AIMD) at 500 K for a 6° tbMoTe_2 using the VASP package⁴⁵. The van der Waals corrections were included using the D2 formalism⁴⁶. More details of NN potential parameterization can be found in ref. 47 The experimental lattice constant of 3.492 \AA was used for the unstrained monolayer, bilayer, and twisted bilayer MoTe_2 ⁴⁸. The band structures were calculated within the SIESTA package⁴⁹. Optimized norm-conserving Vanderbilt pseudopotentials⁵⁰, Perdew–Burke–Ernzerhof functional⁵¹, and double-zeta plus polarization basis were used. The unfolding of moiré minibands into the extended Brillouin zone is performed following the method outlined in ref. 52. To simulate ARPES spectra, a Gaussian smearing is applied to the calculated band structure presented in Fig. 4.

Data availability

The data that support the findings of this study are available from the corresponding author upon reasonable request.

Received: 8 August 2025; Accepted: 6 January 2026;

Published online: 27 January 2026

References

- Geim, A. K. & Grigorieva, I. V. Van der Waals heterostructures. *Nature* **499**, 419–425 (2013).
- Andrei, E. Y. et al. The marvels of moiré materials. *Nat. Rev. Mater.* **6**, 201–206 (2021).
- Nuckolls, K. P. & Yazdani, A. A microscopic perspective on moiré materials. *Nat. Rev. Mater.* **9**, 460–480 (2024).
- Mak, K. F. & Shan, J. Semiconductor moiré materials. *Nat. Nanotechnol.* **17**, 686–695 (2022).
- Kennes, D. M. et al. Moiré heterostructures as a condensed-matter quantum simulator. *Nat. Phys.* **17**, 155–163 (2021).
- Cao, Y. et al. Unconventional superconductivity in magic-angle graphene superlattices. *Nature* **556**, 43–50 (2018).
- Oh, M. et al. Evidence for unconventional superconductivity in twisted bilayer graphene. *Nature* **600**, 240–245 (2021).
- Park, H. et al. Observation of fractionally quantized anomalous Hall effect. *Nature* **622**, 74–79 (2023).
- Cai, J. et al. Signatures of fractional quantum anomalous Hall states in twisted MoTe_2 . *Nature* **622**, 63–68 (2023).
- Xu, F. et al. Observation of integer and fractional quantum anomalous hall effects in twisted bilayer MoTe_2 . *Phys. Rev. X* **13**, 031037 (2023).
- Zeng, Y. et al. Thermodynamic evidence of fractional Chern insulator in moiré MoTe_2 . *Nature* **622**, 69–73 (2023).
- Neupert, T., Santos, L., Chamon, C. & Mudry, C. Fractional quantum hall states at zero magnetic field. *Phys. Rev. Lett.* **106**, 236804 (2011).
- Regnault, N. & Bernevig, B. A. Fractional chern insulator. *Physical Review X* **1**, 021014 (2011).
- Sheng, D. N., Gu, Z.-C., Sun, K. & Sheng, L. Fractional quantum Hall effect in the absence of Landau levels. *Nat. Commun.* **2**, 389 (2011).
- Tang, E., Mei, J.-W. & Wen, X.-G. High-temperature fractional quantum hall states. *Phys. Rev. Lett.* **106**, 236802 (2011).
- Li, Y., Wan, Q. & Xu, N. Recent advances in moiré superlattice systems by angle-resolved photoemission spectroscopy. *Adv. Mater.* **37**, 2305175 (2023).
- Sobota, J. A., He, Y. & Shen, Z.-X. Angle-resolved photoemission studies of quantum materials. *Rev. Mod. Phys.* **93**, 025006 (2021).
- Gao, H. et al. Nano-ARPES endstation at BL07U of Shanghai Synchrotron Radiation Facility. *Synchrotron Radiat. News* **37**, 12–17 (2024).
- Chen, C. et al. Strong electron–phonon coupling in magic-angle twisted bilayer graphene. *Nature* **636**, 342–347 (2024).
- Uri, A. et al. Mapping the twist-angle disorder and Landau levels in magic-angle graphene. *Nature* **581**, 47–52 (2020).
- Utama, M. I. B. et al. Visualization of the flat electronic band in twisted bilayer graphene near the magic angle twist. *Nat. Phys.* **17**, 184–188 (2021).
- Li, Q. et al. Evolution of the flat band and the role of lattice relaxations in twisted bilayer graphene. *Nat. Mater.* **23**, 1070–1076 (2024).
- Pei, D. et al. Observation of Γ -valley moiré bands and emergent hexagonal lattice in twisted transition metal dichalcogenides. *Phys. Rev. X* **12**, 021065 (2022).
- Wilson, N. R. et al. Determination of band offsets, hybridization, and exciton binding in 2D semiconductor heterostructures. *Sci. Adv.* **3**, e1601832 (2017).
- Stansbury, C. H. et al. Visualizing electron localization of WS_2/WSe_2 moiré superlattices in momentum space. *Sci. Adv.* **7**, eabf4387 (2021).
- Ulstrup, S. et al. Direct observation of minibands in a twisted graphene/ WS_2 bilayer. *Sci. Adv.* **6**, eaay6104 (2020).
- Gatti, G. et al. Flat Γ moiré bands in twisted bilayer WSe_2 . *Phys. Rev. Lett.* **131**, 046401 (2023).
- Pei, D. et al. Twist-induced modification in the electronic structure of bilayer WSe_2 . *Nano Lett.* **23**, 7008–7013 (2023).
- Peng, H. et al. Substrate doping effect and unusually large angle van hove singularity evolution in twisted Bi- and multilayer graphene. *Adv. Mater.* **29**, 1606741 (2017).
- Cucchi, I. et al. Microfocus laser–angle-resolved photoemission on encapsulated mono-, bi-, and few-layer $1\text{T}'\text{-WTe}_2$. *Nano Lett.* **19**, 554–560 (2019).
- Zhang, Y. et al. Symmetry engineering in twisted bilayer WTe_2 . *Nano Lett.* **23**, 9280–9286 (2023).
- Wu, F., Lovorn, T., Tutuc, E., Martin, I. & MacDonald, A. H. Topological insulators in twisted transition metal dichalcogenide homobilayers. *Phys. Rev. Lett.* **122**, 086402 (2019).
- Devakul, T., Crépel, V., Zhang, Y. & Fu, L. Magic in twisted transition metal dichalcogenide bilayers. *Nat. Commun.* **12**, 6730 (2021).
- Yuan, H. et al. Evolution of the valley position in bulk transition-metal chalcogenides and their monolayer limit. *Nano Lett.* **16**, 4738–4745 (2016).
- Nguyen, P. V. et al. Field-dependent band structure measurements in two-dimensional heterostructures. *Nano Lett.* **21**, 10532–10537 (2021).
- Gao, S. & Yang, L. Renormalization of the quasiparticle band gap in doped two-dimensional materials from many-body calculations. *Phys. Rev. B* **96**, 155410 (2017).
- Zhao, W. et al. Direct measurement of the electronic structure and band gap nature of atomic-layer-thick 2H-MoTe_2 . Preprint at <https://doi.org/10.48550/arXiv.2001.05894> (2020).
- Madéo, J. et al. Directly visualizing the momentum-forbidden dark excitons and their dynamics in atomically thin semiconductors. *Science* **370**, 1199–1204 (2020).
- Man, M. K. L. et al. Experimental measurement of the intrinsic excitonic wave function. *Sci. Adv.* **7**, eabg0192 (2021).
- Gatti, G. et al. Flat Γ moiré bands in twisted bilayer WSe_2 . *Phys. Rev. Lett.* **131**, 046401 (2023).
- Fan, Xu. et al. Signatures of unconventional superconductivity near reentrant and fractional quantum anomalous Hall insulators. Preprint at <https://doi.org/10.48550/arXiv.2504.06972> (2025).
- Deng, Y. et al. Nonmonotonic band flattening near the magic angle of twisted bilayer MoTe_2 . *Phys. Rev. X* **15**, 041043 (2025).
- Zhang, L. et al. Deep potential molecular dynamics: a scalable model with the accuracy of quantum mechanics. *Phys. Rev. Lett.* **120**, 143001 (2018).
- Zhang, L. et al. DeePMD-kit: a deep learning package for many-body potential energy representation and molecular dynamics. *Comput. Phys. Commun.* **228**, 178–184 (2018).
- Kresse, G. & Furthmüller, J. Efficiency of ab-initio total energy calculations for metals and semiconductors using a plane-wave basis set. *Comput. Mater. Sci.* **6**, 15–50 (1996).
- Grimme, S. Semiempirical GGA-type density functional constructed with a long-range dispersion correction. *J. Comput. Chem.* **27**, 1787–1799 (2006).

47. Zhang, X.-W. et al. Polarization-driven band topology evolution in twisted MoTe₂ and WSe₂. *Nat. Commun.* **15**, 4223 (2024).
48. Agarwal, M. K. & Capers, M. J. The measurement of the lattice parameters of molybdenum ditelluride. *J. Appl. Crystallogr.* **5**, 63–66 (1972).
49. José, M. S. et al. The SIESTA method for ab initio order-N materials simulation. *J. Phys. Condens. Matter.* **14**, 2745 (2002).
50. Hamann, D. R. Optimized norm-conserving Vanderbilt pseudopotentials. *Phys. Rev. B* **88**, 085117 (2013).
51. Perdew, J. P., Burke, K. & Ernzerhof, M. Generalized gradient approximation made simple. *Phys. Rev. Lett.* **77**, 3865–3868 (1996).
52. Mayo, S. G., Yndurain, F. & Soler, J. M. Band unfolding made simple. *J. Phys. Condens. Matter.* **32**, 205902 (2020).

Acknowledgements

We thank Y. Deng, P. Nguyen, H. Park, J. Cai, and T. Li for helpful discussions and the help during sample fabrications. Device fabrication and photoluminescence are supported by the U.S. Department of Energy (DOE), Office of Science, Basic Energy Sciences (BES), under the award DE-SC0012509. Use of the Advanced Light Source, Lawrence Berkeley National Laboratory, is supported by the U.S. Department of Energy, Office of Science under Contract No. DE-AC02-05CH11231. Y.C. and C.C. acknowledge the support from the Oxford-ShanghaiTech collaboration project. K.W. and T.T. acknowledge support from the JSPS KAKENHI (Grant Nos. 21H05233 and 23H02052) and the World Premier International Research Center Initiative, MEXT, Japan.

Author contributions

Y.C. and X.X. conceived and supervised the project. W.H. fabricated the sample devices. C.C., S.H., J.L., and Y.G. performed the ARPES measurements. E.A., Y.Z., and W.L. performed optical measurements. X.Z., T.C., and D.X. performed theoretical calculation. C.J., A.B., and E.R. maintained the ARPES beamline. K.W. and T.T. synthesized the hBN crystals. C.C. and Y.C. wrote the paper with input from all authors.

Competing interests

The authors declare no competing interests.

Additional information

Supplementary information The online version contains supplementary material available at <https://doi.org/10.1038/s42005-026-02497-8>.

Correspondence and requests for materials should be addressed to Yulin Chen.

Peer review information *Communications Physics* thanks the anonymous reviewers for their contribution to the peer review of this work.

Reprints and permissions information is available at <http://www.nature.com/reprints>

Publisher's note Springer Nature remains neutral with regard to jurisdictional claims in published maps and institutional affiliations.

Open Access This article is licensed under a Creative Commons Attribution-NonCommercial-NoDerivatives 4.0 International License, which permits any non-commercial use, sharing, distribution and reproduction in any medium or format, as long as you give appropriate credit to the original author(s) and the source, provide a link to the Creative Commons licence, and indicate if you modified the licensed material. You do not have permission under this licence to share adapted material derived from this article or parts of it. The images or other third party material in this article are included in the article's Creative Commons licence, unless indicated otherwise in a credit line to the material. If material is not included in the article's Creative Commons licence and your intended use is not permitted by statutory regulation or exceeds the permitted use, you will need to obtain permission directly from the copyright holder. To view a copy of this licence, visit <http://creativecommons.org/licenses/by-nc-nd/4.0/>.

© The Author(s) 2026